HITTITE JOURNAL OF SCIENCE AND ENGINEERING

e-ISSN: 2148-4171
Volume: 12 • Number: 1
March 2025

High Temperature Oxidation of Y doped Equiatomic AlCrFeNi Medium Entropy Alloy

Kerem Özgür Gündüz
Gebze Technical University, Materials Science and Engineering Department, Kocaeli, Türkiye.

Corresponding Author
Kerem Özgür Gündüz
E-mail: gunduz@gtu.edu.tr Phone: +90 262 605 26 65 Fax: +90 262 605 26 70
RORID: https://ror.org/01sdnnq10

Article Information
Article Type: Research Article
Doi: https://doi.org/10.17350/HJSE19030000348
Received: 11.11.2024
Accepted: 27.01.2025
Published: 25.03.2025

Cite As
Gündüz ÖK. High Temperature Oxidation of Y doped Equiatomic AlCrFeNi Medium Entropy Alloy. Hittite J Sci Eng. 2025;12(1):25-34.

Peer Review: Evaluated by independent reviewers working in at least two different institutions appointed by the field editor.
Ethical Statement: Not available.
Plagiarism Checks: Yes - iThenticate
Conflict of Interest: Authors declare no conflict of interest.

CRediT AUTHOR STATEMENT
Kerem Özgür Gündüz: Conceptualization, Data curation, Formal Analysis, Investigation, Methodology, Resources, Supervision, Writing – review and editing.

High Temperature Oxidation of Y doped Equiatomic AlCrFeNi Medium Entropy Alloy

Kerem Özgür Gündüz

Gebze Technical University, Materials Science and Engineering Department, Kocaeli, Türkiye.

Abstract

High temperature oxidation (HTO) of Y-doped (0.08 at.%) equiatomic AlCrFeNi alloy produced by vacuum arc melting was studied at 1100 °C for 168h in dry air. As-cast alloys consisted of disordered Fe-Cr rich A2 and Ni-Al rich B2 phase with the additional Y-rich precipitates rich in Ni and Al resembling B2 phase. Alloys possessed a columnar-dendritic microstructure in which dendritic regions contained weave-like morphology (≈120 nm), while interdendritic regions contained relatively coarse structures. Y-rich coarse precipitates were mostly found to segregate into interdendritic regions. After HTO tests the only oxide phase found was α-Al_2O_3 and lower mass gains compared to undoped material were recorded (lean≈ 0.95 mg.cm^{-2}, Y-doped 0.83 mg.cm^{-2}). Two distinct regions were observed based on top-view investigations I) Y-rich regions coupled with smooth Al_2O_3, II) Y-poor regions containing whiskers and smooth Al_2O_3. In both cases, wrinkling of Al_2O_3 scales was not observed. No oxide spallation was observed except at the edges. Additional stress formation on the edges coupled with the high strength of the alloy is assumed to result in oxide spallation. Compact Al_2O_3 scales exhibiting planar metal-oxide interface without wrinkles were observed by cross-sectional analysis. Y/Al-rich precipitates were found within the oxide scale and within the alloy (internal oxidation). Exposing samples also resulted in coarsening of A2 and B2 phases yet the alloy experienced only a 10% reduction in Vickers microhardness values (398 ± 6.8 HV). More studies on optimization of reactive element doping as well as mechanical properties are needed for further improvement of HTO performance.

Keywords: Medium Entropy Alloy, High Temperature Oxidation, Reactive elements, AlCrFeNi, Spallation

INTRODUCTION

Owing to their superior high temperature oxidation (HTO) resistance, ferritic FeCrAl alloys containing 13-20 wt. %Cr and 5-6 wt.% Al are widely used as heating elements in furnaces, cladding materials in nuclear industry, substrates in automobile exhaust catalysts and many more (1–3). This superior HTO resistance of FeCrAl alloys is related with the slow-growing protective α-Al_2O_3 scale especially over 900 °C and can be utilized up to 1300 °C (4,5). However, lean Al_2O_3 forming alloys without de-sulfurization are susceptible to spallation especially when exposed in cyclic oxidation conditions (6). Therefore, these alloys are commonly doped with reactive elements such as Y, Zr, Hf, La, Ce and their oxides (Y_2O_3, ZrO_2) to improve oxide adhesion and slow down the Al_2O_3 growth rate (7,8). The latter not only improves the oxidation properties, but also improves the mechanical properties (e.g. creep resistance) (7,8). Despite their excellent HTO resistance, FeCrAl alloys with open body BCC structure do not possess the desired mechanical properties at elevated temperatures (>600 °C) which highly restrict their applicability (9). Oxide dispersion strengthened (ODS) FeCrAl alloys with better mechanical properties are commercially available (e.g. Kanthal APMT), but they are expensive due to manufacturing route (powder metallurgy) (9). Hence, affordable alloys with identical HTO resistance but with better mechanical properties are needed. One such alternative might be cost effective Co free AlCrFeNi medium entropy alloys (ΔS_{con}: R>x>1.5R). This group of alloys either in equiatomic or in non-equiatomic compositions were shown to form α-Al_2O_3 scales at elevated temperatures (T≥900 °C) with much better mechanical properties such as high yield strength (1041-1424 MPa), high microhardness (403-553 HV) and adequate compressive ductility (ε≈ 18.6-40%) (10–16). Better mechanical properties of these alloys are related with the two-phase structure, B2 phase (Ni-Al rich) reinforcing A2 phase (Fe-Cr rich) (11). However, based on previous studies, RE-free AlCrFeNi alloys especially at 1100 ºC formed wrinkled/buckled α-Al_2O_3 scales with equiaxed morphology and showed extensive oxide spallation which will without a doubt limit the lifetime of these alloys in HTO conditions (14,16). Hence, improvement of high temperature oxidation properties by reactive element modification is needed on AlCrFeNi alloys. Y is one such element and studied extensively to modify FeCrAl and AlCoCrFeNi alloys as a single dopant (6,7,17,18). Y and Y_2O_3 modification are also studied on Cr_2O_3 forming CrFeNi and CoCrFeNi medium entropy alloys not only for improving the oxidation properties but also for better thermal stability (19–22). Especially on FeCrAl alloys, when used as a single dopant, 0.08 at.% Y addition was found to be most effective for prolonging the life time at elevated temperatures (7). However, to the best of the authors knowledge, the effect of reactive element doping on Co-free AlCrFeNi alloys are not yet studied. Therefore, for the first time, high temperature oxidation of Y-doped (0.08 at. % Y) equiatomic AlCrFeNi alloy at 1100 ºC for 168h is studied under air.

MATERIAL AND METHODS

Production and Characterization of Alloys

Y doped medium entropy AlCrFeNi alloy with the nominal composition of $Y_{0.08}$-$Al_{24.98}$ $Cr_{24.98}Fe_{24.98}Ni_{24.98}$ was produced by vacuum arc melting method (Edmund Bühler GmbH, Arc Melter AM200). Hereinafter, the alloy will be designated as Y-AlCrFeNi. Metals at least %99.95 pure were used to produce the alloys. Prior to melting, the chamber was evacuated to 10^{-6} mbar and subsequently filled with Ar (%99.999 pure). Final gas pressure of the system was 600 mbar. Melting process was carried out in two steps. First, Fe-Y master alloy containing 1 at.% Y was prepared. In the second step, this master alloy was melted with pure elements together to fabricate the alloy according to the nominal composition given previously. To obtain homogenous castings, alloys were melted at least 5 times by flipping them upside down in each melting cycle. Final castings were in the shape of ingots with the dimensions of 50 mm x 10 mm x 10 mm. Total weight of ingots after vacuum melting were approximately 24g. To obtain samples with the dimensions of 10 mm x 10 mm x 1 mm, ingots were sectioned with a low-speed saw. After sectioning, samples were ground down to 2500 grit emery paper and subsequently polished with alumina suspension (≈1 µm particle size). After polishing, samples were etched with 3 parts of HCl, 1 part of HNO_3 and

2 parts of H_2O for further metallographic investigations. It should be mentioned that only polished samples were used in high temperature oxidation tests. Prior to oxidation tests, phase analysis was carried out by Bruker D8 Advance (Cu Kα radiation) diffractometer by scanning between 20°-90° with the step size of 0.02°. The scanning rate was selected as 2 °/min and the electrical parameters were 40 mA and 40 kV. Microstructural investigations were made by Nikon Eclipse LV150 light microscope and Philips XL30 FEG SEM equipped with EDS detector (Amatek EDAX). Microhardness tests (Vickers) were carried out with Instron Wolpert Testor 2100 device under 500g load for 5 seconds of loading, dwell and unloading time. ASTM standard E92 is used as the microhardness procedure which is valid between 200gf-150kgf.

High Temperature Oxidation Tests

High temperature oxidation tests were carried out in tube furnace at 1100 °C under laboratory air for 168h. This temperature and exposure duration is commonly practiced to understand the initial high temperature oxidation behavior of Al_2O_3 forming alloys (23,24). Relative humidity of the room was approximately 25%. Temperature profiling of the furnace was carried out by placing an external IN625 jacketed k-type thermocouple in the furnace. The hottest zone of the furnace was approximately 10 cm long and temperature within this zone deviated ± 4 °C. Heating and cooling rate of the samples were 5 °C/min. Samples were placed in Al_2O_3 crucibles (%99.8 purity) in a way to achieve minimum contact with the sample. To ensure reproducibility of the results, exposures were repeated twice and 3 samples were exposed in each oxidation test. Mass gains for each sample was determined by weighing samples before and after HTO tests using sartorius CPA225D scale. The resolution of the scale is 0.01 mg.

Characterization After High Temperature Oxidation Tests

After HTO tests, phase analysis was carried out by Bruker Advance D8 diffractometer with identical parameters used to characterize as-cast alloys. After XRD analysis, top view investigations were made by Philips XL 30 FEG SEM equipped with Amatek EDAX EDS detector. Before SEM investigations, samples were deposited with gold to prevent charging. For cross-sectional investigations one sample was cold mounted with epoxy resin (Struers Epofix) without sectioning. Cold mounted samples were ground down to 2500 grit emery paper and subsequently polished with colloidal Alumina (≈1 µm) and Silica (≈50 nm). Cross-sectional SEM-EDS examinations were also made with Philips XL30 FEG SEM. Samples were also deposited with gold before the cross-sectional investigations. Microhardness tests were also made with the same device with identical parameters.

RESULTS AND DISCUSSION

Investigation of as-cast Y-AlCrFeNi Alloy

Figure 1 illustrates the XRD analysis of as-cast Y-AlCrFeNi alloy. According to the analysis, two phases were detected. I) Fe-Cr rich disordered BCC A2 phase and II) and Ni-Al rich ordered BCC B2 phase. Y-rich phase if present any were not found in the diffractogram most probably related to the minor dopant concentration (0.08 at. %Y) in the alloy. Additionally, peaks of A2 and B2 phases were found to overlap in the diffractogram since these phases have very similar lattice parameters (11). Yet, the (111) peak observed at 55° only belongs to B2 phase, hence justifies the presence of B2 phase (25,26). Furthermore, a second XRD analysis was performed on the same alloy by grinding and re-analyzing the surface and the obtained diffractogram is presented in the supplementary information as Figure S1. B2 phase is usually characterized with the (100) reflection. After the second XRD analysis, both (100) peak with the additional (111) was observed in the diffractogram hence proving the presence of B2 phase. Similar XRD results on AlCrFeNi alloys were also given in previous studies (25–28). The intensity of (110) peak is much higher compared to the other peaks observed in the XRD diffractogram. In contrast, in the second diffractogram the intensity of (211) peak was much higher (Figure S1). The reason for that is related to the production route, since alloys produced by vacuum arc melting usually exhibit anisotropic microstructures due to directional and slow solidification process (16,25,28).

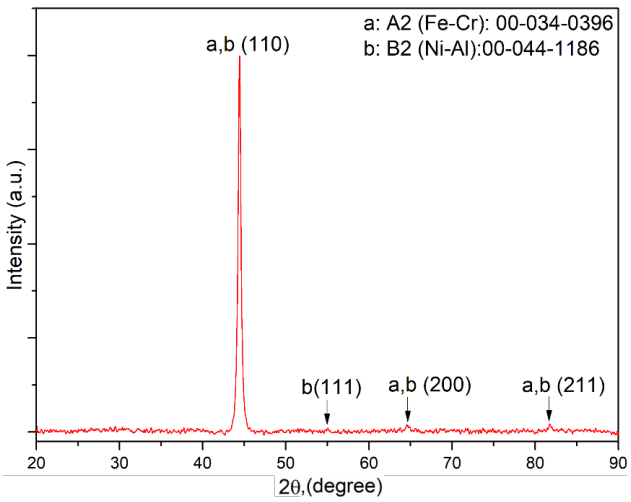

Figure 1: XRD pattern of as-cast Y-AlCrFeNi alloy.

Figure 2 represents the SEM images of polished as-cast Y-AlCrFeNi alloys captured with BSE detector with different magnifications. According to low-magnification images, columnar grains with different orientations were revealed by electron channeling contrast. However, etched optical microscopy images given in Figure S2 (supplementary information) revealed that, the microstructure is dendritic. Hence, orientation difference should be related to the formation of dendrites in a columnar manner with different orientations during the solidification process. General composition of Y-AlCrFeNi alloy determined by SEM-EDS analysis was given in Table 1. Alloys were slightly richer in Al but except that they are very close to the nominal composition. Y concentration was not determined by SEM-EDS analysis due to low Y concentration (0.08 at.% Y). Better analytical techniques such as arc/spark optical emission spectroscopy (OES) or glow discharge optical emission spectroscopy (GD-OES) is needed to determine the actual Y concentration. Furthermore, magnified images Figure 2b and

Figure 2c revealed that dendritic regions consisted of a two-phase lamellar structure commonly referred as weave-like morphology, dark phase being Ni-al rich B2 phase and bright phase being Fe-Cr rich A2 phase (29,30). The width of lamella in dendritic regions is approximately 120 nm. Interdendritic regions were also consisted of same phases, yet they are coarser and resemble a cellular morphology (≈ 1µm). On dendritic regions, it is impossible by SEM-EDS to determine the chemical composition of these phases individually due to small lamella size. However, SEM-EDS analysis carried out on interdendritic regions (Table 1), clarified that dark regions are Ni-Al rich while bright regions are rich in Fe-Cr. The region where the chemical analysis of individual A2 and B2 phases determined by SEM-EDS were given in the supplementary information section as Figure S3. Based on TEM analysis performed in previous studies, the dark regions correspond to Ni-Al rich B2 phase while bright regions correspond to Fe-Cr rich A2 phase (13,28). There is a slight difference in compositions between SEM-EDS and TEM-EDS due to fine microstructure coupled with relatively low spatial resolution of SEM-EDS despite performing the analysis the on coarse regions. Furthermore, In the same Figure (Figure S3), some bright precipitates were observed within the coarse B2 phase located at the interdendritic regions. Due to the very small size of these precipitates, it was not possible to identify these with SEM-EDS analysis, hence further work is needed with TEM-EDS or Atom Probe Tomography (APT). Yet, a study performed on AlCrFeNi system identified these precipitates as A2 precipitates within the B2 coarse matrix (30). Hence, it is likely that these are A2 precipitates. More will be discussed in the upcoming sections.

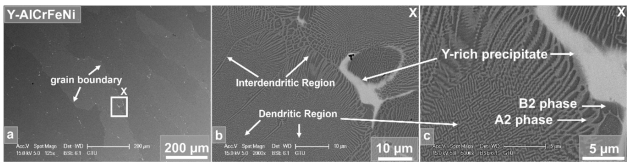

Figure 2. SEM analysis of as-cast Y-AlCrFeNi alloy. a) 125x magnification while b) 2000x and c) 5000x are magnified images of region X marked in a).

Additionally, Y-rich bright precipitates were found to be distributed in the microstructure, as coarse precipitates mostly segregated into interdendritic regions. Y-rich precipitates did not have a distinct morphology, yet the width of these precipitates is approximately 1-5 µm. Chemical analysis of these precipitates by SEM-EDS is also given in Table 1. Based on the obtained composition, these precipitates resemble Ni-Al rich B2 phase enriched with Y. Further analysis is needed to determine this by SEM-EBSD or TEM-SAED. Still, according to previous research on Y doped AlCoCrFeNi alloy, a new phase is identified as a Ni-Y rich phase differing from the Ni-Al phase, but the chemical composition of this phase is not given (31). It is possible that, same phase might be present in the current study. Nevertheless, more studies are needed for phase identification of Y-rich precipitates.

Table 1. SEM-EDS analysis results of as-cast Y-AlCrFeNi.

Points	Fe	Cr	Al	Ni	Y
General Composition	24.36	24.05	27.2	24.39	-
A2 Phase	39.71	43.55	9.77	6.97	-
B2 Phase	15.67	12.54	33.89	37.9	-
Y-Rich Precipitate	9.35	4.35	30.5	41.81	13.99

Furthermore, as-cast Y-AlCrFeNi alloy exhibited a microhardness value of 447 ± 17 HV. A2 and B2 phases exhibit very similar lattice parameters hence they form coherent interfaces which can be understood from the overlapping of peaks in the XRD diffractogram (28,32). The misfit strain in weave-like A2/B2 structures in AlCoCrFeNi alloys were reported as ε= 0.7% (33). This high misfit strain in return causes hardening but in the cost of ductility(29,30). Nevertheless, obtained values are consistent with the previous publications on equiatomic AlCrFeNi alloys (12,13,16). Furthermore, when compared, this value is twice as much of FeCrAl alloys which in return might increase the applicability for load bearing high temperature applications (34). However, as a future work, it is intended to produce alloys with lower misfit strains to achieve a balance between hardness and ductility.

Investigations After High Temperature Oxidation Tests

Figure 3 represents the XRD analysis of Y-AlCrFeNi alloy after HTO tests at 1100 °C after 168h. According to the diffractogram, the only phase detected after the HTO tests are α-Al_2O_3 showing the capability of Y-AlCrFeNi alloy to form protective α-Al_2O_3 scale. No additional phase containing Y-rich oxides were detected in the XRD analysis presumably due to low concentration of Y (0.08 at.% Y) in the alloy. According to the study of Ren et al. (31) when AlCoCrFeNi is doped with 0.1 at.% Y, the only detected phase was also α-Al_2O_3. Tang et al. (18) also reported similar results. Therefore, results consist well with the previous studies. Furthermore, additional peaks belonging to alloy phases (A2 and B2) were also observed. Peaks observed at 2θ= 25° and 44.2° were not able to be identified hence designated as X.

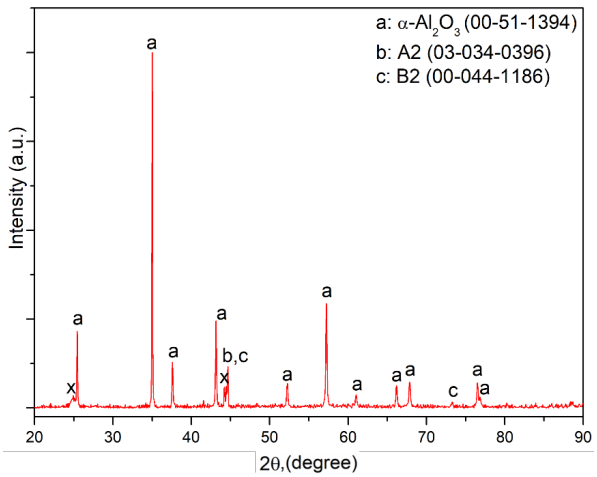

Figure 3. XRD analysis of oxidized Y-AlCrFeNi alloys at 1100 °C for 168h in dry air.

Figure 4. illustrates the top-view SEM images captured after oxidation tests at 1100 °C for 168h. Images Figure 4b and Figure 4c are the magnified regions shown in Figure 4a. Furthermore, Figure 5 represents the point SEM-EDS analysis carried out on regions X and Y marked in Figure 4. Point analysis results are given in Table 2. According to the combined results of Figure 4 and Figure 5, two distinct regions were identified. X represents regions containing whiskers and flat surfaces while region Y consists of bright oxides coupled with flat surfaces without formation of whiskers. On region X, SEM-EDS results suggest the presence of Al_2O_3 based on the analysis carried out on whiskers and flat surfaces. On the other hand, bright oxides found in region Y suggest the formation of a Y and Al rich oxide, coupled with the formation of Al_2O_3. The chemical composition and related phases will be discussed in cross-sectional SEM-EDS examinations.

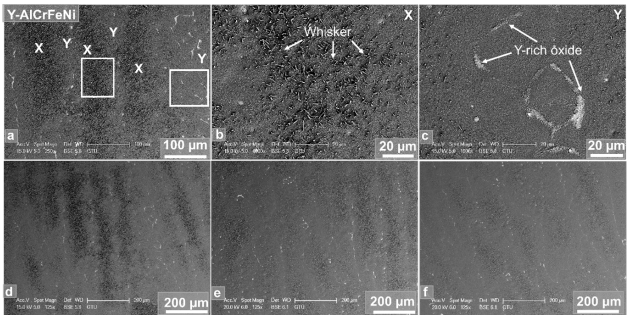

Figure 4. Top-View SEM images of Y-AlCrFeNi alloys after oxidation at 1100 °C for 168h. a) Low magnification top view image. b) Region marked as X in low magnification image. c) Region marked as Y in low magnification image. Images d), e), f) represent alternative images showing that regions X and Y is repeating all over the surface.

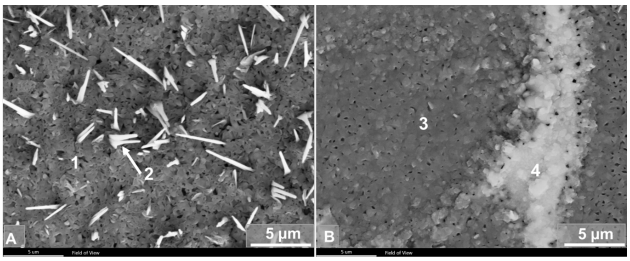

Figure 5. Top-view point SEM-EDS analysis of oxidized Y-AlCrFeNi carried out on a) whisker rich regions and b) Y-rich oxide regions.

Table 2. Top-view point SEM-EDS analysis results of regions marked in Figure 5.

Points	Fe	Cr	Al	Ni	Y	O
1	0.34	0.41	47.61	0.08	0.11	51.45
2	0.18	0.21	36.99	0.05	0.06	62.51
3	0.31	0.66	46.66	0.11	0.13	52.14
4	2.8	1.32	33.23	5.44	9.45	47.76

Furthermore, Figures 4d-4f clearly show that the oxidation pattern observed in Figure 4a is repeated everywhere on the surface: Whiskers being formed on regions that do not contain Y-rich oxides, while the presence of Y-rich oxides suppressed whisker formation. The presence of whiskers on the surfaces is due to formation of metastable Al_2O_3 phases such as θ-Al_2O_3 or γ-Al_2O_3 which are not protective and grow outwards by cation diffusion(35–37) . With time, they do transform into α-Al_2O_3 (38). The important conclusion is the presence of Y-rich oxides clearly shown to suppress whisker formation at 1100 °C when compared with the lean equiatomic AlCrFeNi alloy (16). This is also verified on after oxidation top-view analysis of Y doped FeCrAl alloys (37,39). In fact, on FeCrAl alloys, due to homogeneous distribution of Y-rich precipitates in the matrix, whisker formation is eliminated (37,39). However, arc melted Y-AlCrFeNi alloy did not show this effect, since Y-rich coarse precipitates were mostly segregated into interdendritic regions and in return, Y-rich oxides were more regularly formed in these regions after high temperature oxidation. Therefore, the effect of suppressing whisker formation is rather localized in vacuum arc melted Y-AlCrFeNi alloy. By investigating the previous studies on Y doped AlCrCoFeNi alloys, no such oxidation behavior (regions with and without whiskers) was reported (18,31,40). One such possibility might be the heating regime. Rather than placing the samples in the cool furnace and ramping with a typical heating rate of 5-7 ºC/min, directly inserting the samples into hot zone of the pre-heated furnace at 1100 °C might have mitigated the formation of whiskers since over 1000 °C formation of metastable Al_2O_3 phases are greatly suppressed (35).

Nevertheless, compared to lean equiatomic AlCrFeNi alloy, spallation free, smooth Al_2O_3 scales without any wrinkling were obtained on Y-AlCrFeNi alloy even on the whisker containing regions, showing the beneficial effect of Y doping (16). However, additional top-view SEM images captured on the edges of oxidized samples given in Figure 6 show that Al_2O_3 scales on the edges were completely spalled off, revealing the bare alloy surface. Since the metal surfaces revealed by oxide spallation do not contain any newly formed oxide, it is suggested that Al_2O_3 scales spalled off during the cooling step. The reason for such behavior is related to the additional stress formation on the edges due to geometrical effect coupled with the high strength of Y-AlCrFeNi alloy. All high temperature alloys, when oxidized at elevated temperatures, experience additional stress formation on the edges due to their high curvature (sharp edges) (41,42). Yet, alloys with weak mechanical properties such as FeCrAl alloys, especially at elevated temperatures, can relieve these additional stresses by the combined plastic deformation of alloy and oxide (8). However, the high strength of Y-AlCrFeNi alloy similar to ODS FeCrAl alloys hinders the plastic deformation of alloy thus stress is relieved by the fracture and spallation of Al_2O_3 scales (8,43). Spallation of oxides around edges were also reported in HTO of lean equiatomic AlCrFeNi alloy at 1100 ºC (16). To the best of the authors knowledge, edges of Y-doped AlCrCoFeNi alloys (similar mechanical properties to AlCrFeNi alloy) after high temperature oxidation were not investigated (18,31,40). As a future study, it might be interesting to examine how edges of Y doped AlCoCrFeNi alloys behave after high temperature oxidation. Figure 7 depicts the cross-sectional SEM images captured after high temperature oxidation tests at 1100 °C for 168h. Figure 8 illustrates the SEM-EDS elemental mapping results while Figure 9 shows the point SEM-EDS analysis results. Point SEM-EDS results were tabulated in

Table 3.

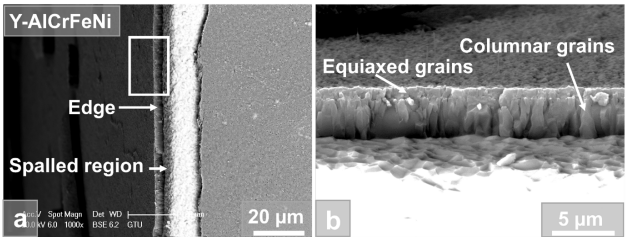

Figure 6. Top-view SEM analysis of oxidized Y-AlCrFeNi alloy captured near the edges of the sample, a) low magnification image, b) Marked region in image a in higher magnification.

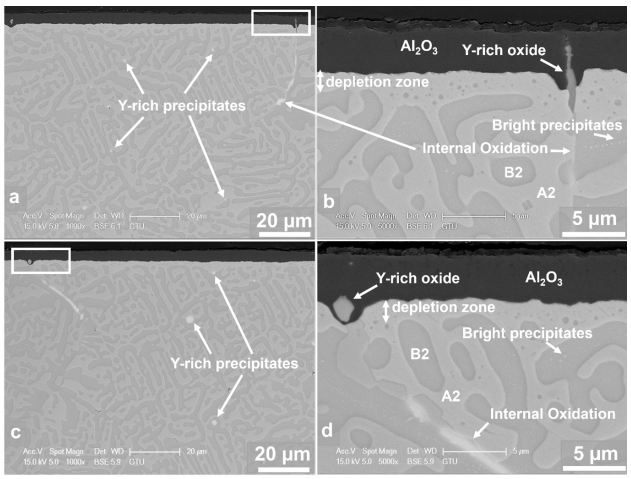

Figure 7. Cross-sectional SEM images of oxidized Y-AlCrFeNi alloy captured from two different regions, a,c) low magnification images , b,d) High magnification images of regions marked in a), c) respectively.

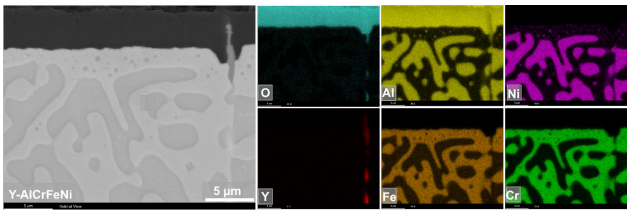

Figure 8. Cross-sectional SEM-EDS Mapping analysis of oxidized Y-AlCrFeNi alloy.

Table 3. Cross sectional point SEM-EDS analysis results of regions marked in Figure 9.

Points	Fe	Cr	Al	Ni	Y	O
1	-	-	43.24	-	-	56.76
2	-	-	33.29		8.8	57.91
3	-	-	43.47	-	-	56.53
4	-	-	25.47	-	15.35	59.18
5	43.71	48.43	4.82	3.04	-	-
6	8.92	4.07	43.55	43.46	-	-
7	9.8	3.15	26.77	46.34	13.94	-
8	9.43	3.68	26.54	46.45	13.9	-

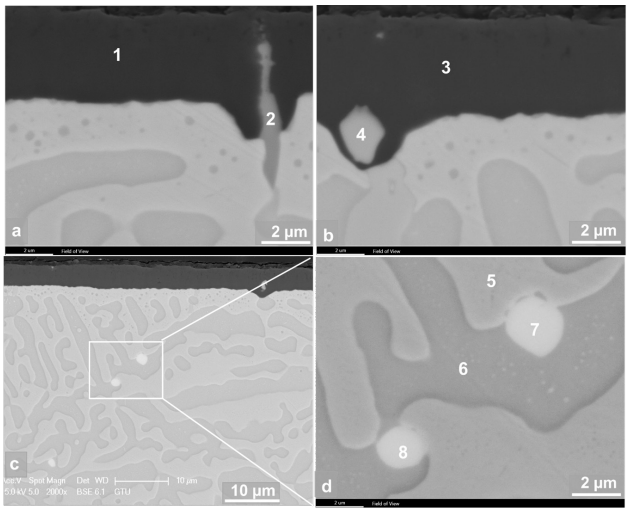

Figure 9. Cross-sectional point SEM-EDS analysis of oxidized Y-AlCrFeNi alloy. a,b) Different regions containing Y-rich oxides, c) Region that contains Y-rich precipitates in the alloy. d) Marked region of Figure c in higher magnification.

Based on the cross-sectional analysis combined with XRD results, pore free α-Al_2O_3 scales with planar metal-oxide interfaces without wrinkles/buckles were obtained. α-Al_2O_3 scales also adhered well to the substrate. When compared with the lean equiatomic AlCrFeNi alloy, this is a significant improvement showing the beneficial effect of Y addition (16).

In localized regions though, Y-Al rich oxides were also present as coarse precipitates within the oxide due to relatively high Y concentration (Figure 8 and Figure 9). In some cases, they were completely encapsulated within the oxide scale. When they are located around the metal-oxide interface they form localized inwards grown perturbations/intrusions known as oxide pegs (44,45). In earlier studies, oxide pegs were reported to improve oxide adhesion by mechanical keying the oxide scale to the substrate. However, present studies show that it is not necessary to have oxide pegs to improve the adhesion of oxide scales (44,46).

Alternatively, when Y-Al rich precipitates are not enveloped continuously by Al_2O_3 scale, the oxidation is progressing towards the metal, forming internal oxides especially in metal grain boundaries (intergranular oxidation). In other words, these precipitates act as oxygen channels towards the metal (17). These internal oxides are reaching almost 50 µm deep within the metal. Based on previous studies, these Y-Al precipitates within oxide scale are identified as Yttrium Aluminates. In high temperature oxidation studies, most commonly observed Yttrium Aluminate phase is $Y_3Al_5O_{12}$ (YAG phase) along with the $YAlO_3$ (YAP phase) (17,47,48). Point analysis performed on the Y-Al rich precipitate observed in Figure 9b showed excellent fit to $Y_3Al_5O_{12}$ phase (Point 4 in Table 3). Yet, the precipitate observed in Figure 9a showed a darker contrast and measured to be richer in Al (Point 2, Table 3). None of the phases reported in the Y_2O_3-Al_2O_3 phase diagram fit into this stoichiometry (49). Additionally, it should be stated that, this precipitate has

an elongated rod-like shape hence it is possible that signals might have been collected from the surroundings during the SEM-EDS analysis. Nevertheless, the darker contrast of this precipitate points toward a relatively Y-poor phase. Further studies with better analytical techniques such as TEM or APT are required to fully identify this phase. Additionally, the deepest part of the mentioned precipitate within the metal (intergranular oxide in the metal) is identified as Y_2O_3 (Figure S4 in the supplementary information) by SEM-EDS analysis which is expected since Y_2O_3 is thermodynamically more stable than Al_2O_3 (17). A very thin depletion zone (≈ 1-2 µm) was observed beneath the Al_2O_3 scale, showing that the alloy can supply sufficient Al to the surface (Figure 9). When compared with the initial microstructure, coarse A2 (bright) and B2 (dark) phases with intertwined morphology were observed in cross-sectional investigations (Figure 9). Point analysis carried out on A2 and B2 precipitates verified that A2 phase is rich in Fe and Cr while B2 phase is rich Ni and Al as expected (Figure 9d and Table 3). The chemical composition of these phases correlates well with the previous studies (13,16,28). Additionally, Y-rich precipitates were also present within the alloy microstructure. Chemical composition of Y-rich precipitates before and after the oxidation tests are quite similar showing that they are rich in Ni, Al and Y. As mentioned previously, these precipitates resemble B2 phase composition that is rich in Y. Yet, further studies with TEM are required to identify the crystal structure of these precipitates. Furthermore, bright precipitates were found within the B2 phase as in the case of coarse structures found in the as-cast alloy (Figure S3). Analysis of such precipitates are given in the supplementary information Figure S5. According to Figure S5, the analysis performed on these regions resulted in a higher Fe/Cr concentration compared to the surrounding regions. Obviously, signals will be collected from the surroundings, yet similar precipitates were identified as A2 phase in a previous study (30). According to previous studies, it is stated that formation of weave-like structure is a result of spinodal decomposition (29,33). Hence a similar mechanism might trigger the formation of nano-precipitates within the B2 phase due to relatively high Fe/Cr concentration of B2 phase. After high temperature oxidation test (1100 °C, 168h), average mass gain values of 0.83 ± 0.01 $mg.cm^{-2}$ were obtained. When compared to the lean Al_2O_3 forming AlCrFeNi alloy (mass gain ≈ 0.95 $mg.cm^{-2}$), and lean FeCrAl alloys at 1100 °C after 1 week (mass gain ≈ 1 $mg.cm^2$), recorded value in the present study is lower (16). It should be noted that the mass gain value for lean equiatomic AlCrFeNi alloy is obtained by converting the thickness value (5.1 ± 0.5 µm) into mass gain to obtain a more accurate value. The reason for obtaining lower mass gain is related to the reduced oxide growth rate and partial elimination of whisker formation when compared with the lean AlCrFeNi alloy (16). However, when compared with the FeCrAl alloys containing 0.1 wt.% Y these values are slightly higher (≈0.76 $g.cm^{-2}$) (37,39). A comparison of surfaces formed on Y-FeCrAl and Y-AlCrFeNi suggests that Y-rich oxides as spherical precipitates were distributed more homogenously on Y-FeCrAl alloy and as a result, formation of whiskers were eliminated with 0.1 wt.% Y doping (37). High entropy AlCoCrFeNi alloys doped with 0.1 at.% Y showed mass gain values around 0.77 $mg.cm^{-2}$ in which whisker formation was not reported (31,40). In the present study, the oxide thickness based on cross-sectional investigations were determined as 3.9 ± 0.14 µm. Conversion of this thickness value into mass gain according to the formula given in reference (50) results in 0.75 $mg.cm^2$. Two sources are identified that results in additional mass gain: I) Formation of Whiskers II) Formation of Y-rich oxide precipitates both in the oxide scale and in the metal (internal oxidation). Since Y-rich oxide formation is also observed on Y-AlCoCrFeNi and Y-FeCrAl alloys, the reason for further additional mass gain is more likely related to the formation of whiskers on top of the oxide scales. Additionally, microhardness measurements carried out after the oxidation tests showed that, values were determined as 398 ± 6.8 HV. Comparing this value with the as-cast structure revealed that the reduction by precipitate coarsening is approximately 10%. Therefore, these alloys were shown to retain their hardness values after 168h at 1100 °C. Prolonged exposures might be useful to observe the coarsening behavior and its effect on microhardness values. Despite Y-AlCrFeNi alloys show enhanced mechanical properties compared to FeCrAl alloys, it seems that high strength of the former caused oxide spallation around edges. This finding shows that the strength of the alloy should be tuned (reduced) by purposeful coarsening with heat-treatments or adjusting the composition in a manner to not prevent plastic deformation at elevated temperatures at least to a level might be a future goal. Additionally, further studies might be useful to improve the high temperature oxidation performance of Co free AlCrFeNi alloys (e.g. mitigating whisker formation or internal oxidation) by optimizing the reactive element concentration, for instance by single doping with Hf and/or double doping with Y and Hf as given in the previous studies (50,51).

CONCLUSION

In this study, production (vacuum arc melting) and high temperature oxidation of Y doped (0.08 at.%Y) cost effective medium entropy AlCrFeNi alloy at 1100 °C for 168h were studied. Conclusions drawn from the present study are given below:

1-Y doped AlCrFeNi alloy in as-cast state consisted of A2 (disordered Fe-Cr rich) and B2 (ordered Ni-Al rich) phases according to XRD and SEM investigations. Due to production by vacuum arc melting, Y-AlCrFeNi alloy was highly oriented in <110> directions.

2-According to etched optical microscopy images coupled with SEM investigations; alloys were found to exhibit a columnar dendritic structure. Dendritic regions consisted of weave-like structures with nano sized A2 and B2 phases while coarser structures with identical phases were found in interdendritic regions. Y-rich coarse precipitates were also observed to form mainly in interdendritic regions. The composition of this phase resembles B2 phase enriched in Y, but further identification with TEM is needed.

3-Microhardness of as-cast Y-AlCrFeNi is measured as 447 ± 11 HV. High hardness of this alloy is due to coherent B2 phase reinforcement of A2 phase.

4-After high temperature oxidation tests carried out at 1100 °C for 168h in dry air, the only detected oxide phase was

α-Al_2O_3 with the additionally observed substrate phases.

5-Top-view analysis revealed that two different types of oxides were observed: I) Region enriched with Y-rich oxides coupled with smooth Al_2O_3 surfaces. II) Y-poor regions consisting of whiskers and smooth Al_2O_3 surfaces. This shows that Y addition into equiatomic AlCrFeNi alloy suppresses whisker formation but not entirely on the surface, due their segregation into interdendritic regions.

6-Despite formation of whiskers on the surface, Y-addition prevented wrinkling and spallation on the main surfaces. However, oxide scales spalled around the edges due to additional stress formation by geometrical effects coupled with the high strength of Y-AlCrFeNi alloy, which prevented stress relaxation by combined plastic deformation of metal and oxide.

7-Cross-sectional investigations revealed that Al_2O_3 scales were compact and pore-free. Planar metal-oxide interfaces without any wrinkles/buckles were observed, verifying the beneficial effect of Y addition.

8-Y-rich precipitates within the oxide scale and within the metal as internally oxidized precipitates were observed in cross-sectional examinations. Some of these precipitates show excellent fit to $Y_3Al_5O_{12}$ (YAG) phase determined by SEM-EDS point analysis. Yet, precipitates deficient in Y were also observed.

9- After exposing samples at 1100 °C for 168h, coarsening of A2 and B2 phases occurred. However, a microhardness value of 398 ± 6.8 HV was measured after the high temperature oxidation tests. Therefore, despite coarsening, only a 10% reduction compared to as-cast structure was obtained.

10-Despite high hardness and its retention after exposures at 1100 ºC for 168h, spallation of oxides located around the edges suggests that an optimization of mechanical properties (heat-treatment, alloying) might be useful for further prolonging the lifetime. Furthermore, optimization of reactive element addition such as double doping with Y and Hf might further improve HTO performance (preventing internal oxidation and whisker formation).

Acknowledgement

Author would like to thank technicians Adem Şen and Ahmet Nazım for their technical assistance in XRD and SEM studies respectively. Casting, sample preparation as well as high temperature oxidation tests were carried out in Gebze Technical University metal casting and heat treatment laboratories, thus the author thanks for the equipment usage to founding members Prof. Dr. Yücel Gençer and Prof. Dr. Mehmet Tarakçı. This work was funded by Gebze Technical University, Project Number: (2023-A-105-01).

References

1. Bunn JK, Fang RL, Albing MR, Mehta A, Kramer MJ, Besser MF, et al. A high-throughput investigation of Fe-Cr-Al as a novel high-temperature coating for nuclear cladding materials. Nanotechnology. 2015;26(27).
2. Naumenko D, Quadakkers WJ, Galerie A, Wouters Y, Jourdain S. Parameters affecting transient oxide formation on FeCrAl based foil and fibre materials. Materials at High Temperatures. 2003 Jan 1;20(3):287–93.
3. Eklund J, Persdotter A, Ssenteza V, Jonsson T. The long-term corrosion behavior of FeCrAl(Si) alloys after breakaway oxidation at 600 °C. Corros Sci. 2023;217:111155.
4. Dryepondt S, Pint BA, Lara-Curzio E. Creep behavior of commercial FeCrAl foils: Beneficial and detrimental effects of oxidation. Materials Science and Engineering: A. 2012;550:10–8.
5. Kim C, Tang C, Grosse M, Maeng Y, Jang C, Steinbrueck M. Oxidation mechanism and kinetics of nuclear-grade FeCrAl alloys in the temperature range of 500–1500 °C in steam. Journal of Nuclear Materials. 2022;564:153696
6. Meier GH, Pettit FS, Smialek JL. The effects of reactive element additions and sulfur removal on the adherence of alumina to Ni- and Fe-base alloys. Materials and Corrosion. 1995 Apr 1;46(4):232–40.
7. Pint BA. Optimization of reactive-element additions to improve oxidation performance of alumina-forming alloys. In: Journal of the American Ceramic Society. 2003.
8. Naumenko D, Pint BA, Quadakkers WJ. Current Thoughts on Reactive Element Effects in Alumina-Forming Systems: In Memory of John Stringer. Vol. 86, Oxidation of Metals. 2016.
9. Brady MP, Yamamoto Y, Santella ML, Maziasz PJ, Pint BA, Liu CT, et al. The development of alumina-forming austenitic stainless steels for high-temperature structural use. JOM. 2008;60(7).
10. Dong Y, Lu Y, Kong J, Zhang J, Li T. Microstructure and mechanical properties of multi-component AlCrFeNiMo x high-entropy alloys. J Alloys Compd. 2013;573.
11. Ren M, Wang G, Li B. Microstructure and properties of AlCrFeNi intermetallic for electronic packaging shell. In: 18th International Conference on Electronic Packaging Technology, ICEPT 2017. 2017.
12. Jiang Z, Chen W, Xia Z, Xiong W, Fu Z. Influence of synthesis method on microstructure and mechanical behavior of Co-free AlCrFeNi medium-entropy alloy. Intermetallics. 2019;108.
13. Jumaev E, Abbas MA, Mun SC, Song G, Hong SJ, Kim KB. Nano-scale structural evolution of quaternary AlCrFeNi based high entropy alloys by the addition of specific minor elements and its effect on mechanical characteristics. J Alloys Compd. 2021;868.
14. Yang D, Liu Y, Han T, Zhou F, Qu N, Liao M, et al. High thermal stability and oxidation behavior of FeCrNiAl-based medium-entropy alloys prepared by powder metallurgy. J Alloys Compd. 2022;918:165562.
15. Hwang YJ, Kim KS, Na YS, Lim KR, Lee KA. High-temperature oxidation properties of economical and lightweight Fe-Cr-Ni-Al medium-entropy alloy. Corros Sci. 2023;219:111231.
16. Ozgenc T, Gunduz KO. Effect of Fe Concentration on the High Temperature Oxidation Behavior of Fex(CrAlNi)100−x Medium Entropy Alloys. High Temperature Corrosion of Materials. 2024;101(2):251–78.
17. Kim S, Lee CH, Kim T, Jang JH, Moon J, Falaakh DF, et al. Effects of yttrium on the oxidation behavior of Fe13Cr6AlY alloys under 1200 °C steam. J Alloys Compd. 2023;960:170642.
18. Tang C, Shi H, Jianu A, Weisenburger A, Victor G, Grosse M, et al. High-temperature oxidation of AlCrFeNi-(Mn or Co) high-entropy alloys: Effect of atmosphere and reactive element addition. Corros Sci. 2021;192.
19. Lu Z, Peng S, Li H, Gao S. Improved oxidation resistance of ODS-CrFeNi medium entropy alloys by different Y2O3/Ti/Zr

additions. J Alloys Compd. 2023;960:171017.
20. Polat G, Kotan H. Microstructural Evolution and Mechanical Properties of Y Added CoCrFeNi High-entropy Alloys Produced by Arc-melting. Hittite Journal of Science and Engineering. 2024;11(1):25–31.
21. Polat G, Tekin M, Kotan H. Role of yttrium addition and annealing temperature on thermal stability and hardness of nanocrystalline CoCrFeNi high entropy alloy. Intermetallics. 2022;146:107589.
22. Tekin M, Polat G, Kalay YE, Kotan H. Grain size stabilization of oxide dispersion strengthened CoCrFeNi-Y2O3 high entropy alloys synthesized by mechanical alloying. J Alloys Compd. 2021;887:161363.
23. Gunduz KO, Visibile A, Sattari M, Fedorova I, Saleem S, Stiller K, et al. The effect of additive manufacturing on the initial High temperature oxidation properties of RE-containing FeCrAl alloys. Corros Sci. 2021;188:109553.
24. Hellström K, Israelsson N, Mortazavi N, Canovic S, Halvarsson M, Svensson JE, et al. Oxidation of a Dispersion-Strengthened Powder Metallurgical FeCrAl Alloy in the Presence of O2 at 1,100 °C: The Influence of Water Vapour. Oxidation of Metals. 2015;83(5):533–58.
25. Singh AK, Subramaniam A. On the formation of disordered solid solutions in multi-component alloys. J Alloys Compd. 2014;587.
26. Tripathy B, Malladi SRK, Bhattacharjee PP. Development of ultrafine grained cobalt-free AlCrFe2Ni2 high entropy alloy with superior mechanical properties by thermo-mechanical processing. Materials Science and Engineering: A. 2022;831:142190.
27. Cui P, Liu Y, Zhou F, Lai Z, Zhu J. Enhancing high temperature mechanical properties via modulating B2 phase with Al contents in FeCrNiAlx(x = 0.63,0.71,0.77) high entropy alloys. J Alloys Compd. 2022;903.
28. Zhou Y, Zhou D, Jin X, Zhang L, Du X, Li B. Design of non-equiatomic medium-entropy alloys. Sci Rep. 2018;8(1).
29. Ma Y, Jiang B, Li C, Wang Q, Dong C, Liaw PK, et al. The BCC/B2 morphologies in Al x NiCoFeCr high-entropy alloys. Metals. 2017;7(2):57.
30. Diao G, Wu M, He A, Xu Z, Mousavi SE, Li D. Manipulate A2/B2 structures in AlCrFexNi alloys for improved mechanical properties and wear resistance. Lubricants. 2023;11(9):392.
31. Ren H, Chen RR, Liu T, Gao XF, Qin G, Wu SP, et al. Unraveling the oxidation mechanism of Y-doped AlCoCrFeNi high-entropy alloy at 1100 °C. Appl Surf Sci. 2024;652:159316.
32. Diao G, Wu M, He A, Xu Z, Bajaj D, Chen D, et al. Adjusting (AlNi)/(FeCr) ratio to tailor microstructure and properties of A2-B2 dual-phase (AlNi)x(FeCr)100-x medium-entropy alloys. Journal of Materials Research and Technology. 2025;34:1921–32.
33. Li JL, Li Z, Wang Q, Dong C, Liaw PK. Phase-field simulation of coherent BCC/B2 microstructures in high entropy alloys. Acta Mater. 2020;197:10–9.
34. Field KG, Snead MA, Yamamoto Y, Terrani KA. Handbook on the material properties of FeCrAl alloys for nuclear power production applications. Nuclear Technology Research and Development. 2017;
35. Berthomé G, N'Dah E, Wouters Y, Galerie A. Temperature dependence of metastable alumina formation during thermal oxidation of FeCrAl foils. Materials and Corrosion. 2005;56(6):389–92.
36. Andoh A, Taniguchi S, Shibata T. TEM observation of phase transformations of alumina scales formed on Al-deposited Fe-Cr-Al foils. In: Materials science forum. Trans Tech Publ; 2001. p. 303–10.
37. Chevalier S, Strehl G, Buscail H, Borchardt G, Larpin JP. Influence of the mode of introduction of a reactive element on the high temperature oxidation behavior of an alumina-forming alloy. Part I: Isothermal oxidation tests. Materials and Corrosion. 2004 May 1;55(5):352–7.
38. Tolpygo VK, Clarke DR. Microstructural study of the theta-alpha transformation in alumina scales formed on nickel-aluminides. Materials at High Temperatures. 2000 Jan 1;17(1):59–70.
39. Issartel C, Buscail H, Chevalier S, Favergeon J. Effect of Yttrium as Alloying Element on a Model Alumina-Forming Alloy Oxidation at 1100 °C. Oxidation of Metals. 2017;88(3–4).
40. Lu J, Zhang H, Chen Y, Li L, Liu X, Xiao W, et al. Y-doped AlCoCrFeNi2.1 eutectic high-entropy alloy with excellent oxidation resistance and structure stability at 1000°C and 1100°C. Corros Sci. 2021;180.
41. Wright JK, Williamson RL, Renusch D, Veal B, Grimsditch M, Hou PY, et al. Residual stresses in convoluted oxide scales. Materials Science and Engineering: A. 1999;262(1):246–55.
42. Evans HE. Stress effects in high temperature oxidation of metals. International materials reviews. 1995;40(1):1–40.
43. Echsler H, Martinez EA, Singheiser L, Quadakkers WJ. Residual stresses in alumina scales grown on different types of Fe–Cr–Al alloys: effect of specimen geometry and cooling rate. Materials Science and Engineering: A. 2004;384(1):1–11.
44. Smialek JL. Invited Review Paper in Commemoration of Over 50 Years of Oxidation of Metals: Alumina Scale Adhesion Mechanisms: A Retrospective Assessment. Oxidation of Metals. 2022;97(1):1–50.
45. Whittle DP, Stringer J. Improvements in high temperature oxidation resistance by additions of reactive elements or oxide dispersions. Philosophical Transactions of the Royal Society of London Series A, Mathematical and Physical Sciences. 1997 Jan 1;295(1413):309–29.
46. Naumenko D, Gleeson B, Wessel E, Singheiser L, Quadakkers WJ. Correlation between the Microstructure, Growth Mechanism, and Growth Kinetics of Alumina Scales on a FeCrAlY Alloy. Metallurgical and Materials Transactions A. 2007;38(12):2974–83.
47. Cueff R, Buscail H, Caudron E, Riffard F, Issartel C, El Messki S. Effect of reactive element oxide coating on the high temperature oxidation behaviour of FeCrAl alloys. Appl Surf Sci. 2004;229(1):233–41.
48. Chevalier S, Issartel C, Cueff R, Buscaif H, Strehl G, Borchardt G. Influence of the mode of introduction of a reactive element on the high temperature oxidation behavior of an alumina-forming alloy. Part III: The use of two stage oxidation experiments and in situ X-ray diffraction to understand the oxidation mechanisms. Materials and Corrosion. 2006 Jun 1;57(6):476–83.
49. 49. Abell JS, Harris IR, Cockayne B, Lent B. An investigation of phase stability in the Y2O3-Al2O3 system. J Mater Sci. 1974;9(4):527–37.
50. 50. Lu J, Chen Y, Zhang H, Ni N, Li L, He L, et al. Y/Hf-doped AlCoCrFeNi high-entropy alloy with ultra oxidation and spallation resistance. Corros Sci. 2020;166.
51. 51. Lu J, Li L, Chen Y, Liu X, Zhao X, Guo F, et al. Y-Hf co-doped AlCoCrFeNi high-entropy alloy coating with superior oxidation and spallation resistance at 1100 °C. Corros Sci. 2021;182:109267.

SUPPLEMENTARY INFORMATION

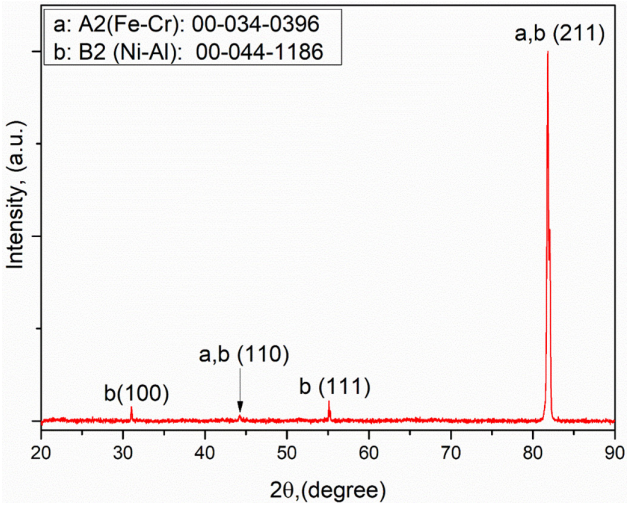

Figure S1. XRD diffractogram of ground and re-analyzed Y-AlCrFeNi alloy.

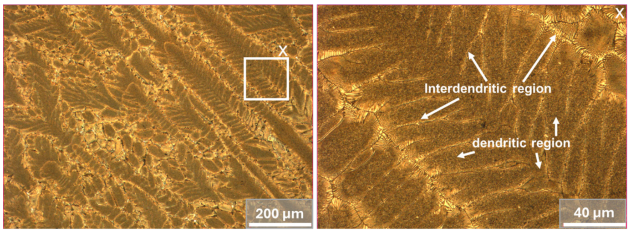

Figure S2. Optical microscope images of etched as-cast Y-AlCrFeNi alloy.

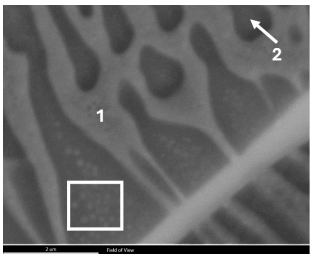

Spot	at.%Fe	at.%Cr	at.%Al	at.%Ni
1(A2)	39.71	43.55	9.77	6.97
2(B2)	15.67	12.54	33.89	37.9

Figure S3. SEM-EDS analysis performed on A2 and B2 phases in the as-cast Y-doped equiatomic AlCrFeNi alloy. Point 1 represents A2 while point 2 represents B2 phase. Note bright precipitates within B2 phase.

Points	Y at.%	Al at.%	O at.%
1	26,86	9.24	63.9
2	35.24	0.87	63.89

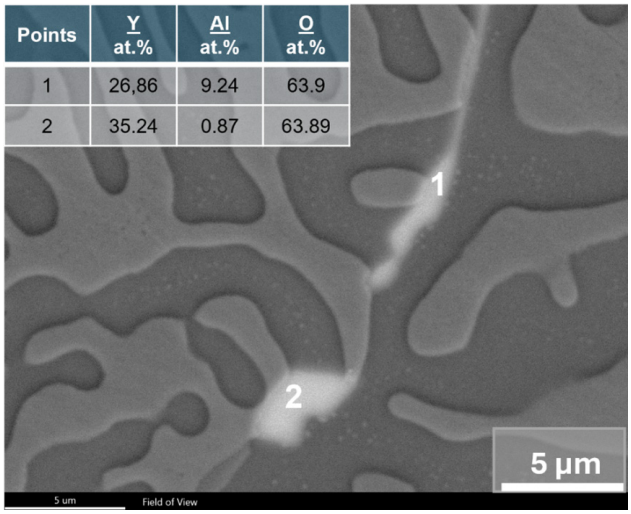

Figure S4. SEM-EDS analysis of internal oxide precipitates located deep within the metal on Y-AlCrFeNi alloy oxidized for 168h at 1100 °C.

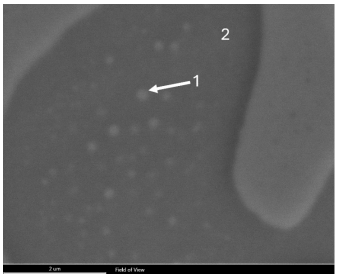

Spot	at.%Fe	at.%Cr	at.%Al	at.%Ni
1	14.77	8.64	39.79	36.8
2	9.09	3.72	43.88	43.31

Figure S5. SEM-EDS analysis performed on bright precipitate (spot 1) and precipitate free region (spot 2) within the B2 phase on the oxidation unaffected region after exposing Y-AlCrFeNi alloy at 1100 °C for 168h.